AIAA JOURNAL
Vol. 34, No. 7, July 1996

Simulating Moth Wing Aerodynamics: Towards the Development of Flapping-Wing Technology

Michael J. C. Smith*
Purdue University, West Lafayette, Indiana 47907-1282

The mechanization of flapping-wing flight is addressed. A tethered moth's flapping wings are simulated using an unsteady aerodynamic panel method and accounts for wing flexibility using a finite element model. The resultant simulation code delineates both the aerodynamic and inertial forces acting on flapping, flexible wings undergoing arbitrary motion in the presence of large-scale vortices and establishes the importance of including the wake in the unsteady analysis of flapping flexible wings. A switching pattern is discovered where the magnitude and direction of the aerodynamic force are decoupled, thereby pointing to a means whereby control is achieved. Overall, important groundwork necessary for the establishment of the principles of flapping-wing flight is laid, leading to the development of a highly agile, alternative flight technology.

Introduction: Rationale for Flapping-Wing Technology Research

THERE is a growing recognized need for more versatile flight vehicles with multifunctional capabilities. The multifunctional trend is evident in designs that either modify existing fixed-wing aircraft (such as the F-18 High Alpha Research Vehicle or the F-16 Multi-Axis Thrust Vectoring) or designs that rely on hybridization and variously combine traditionally distinct technologies in novel ways (such as the Rotary Systems Research Aircraft X-Wing, the Harrier, the V-22 Osprey, and most recently the X-32). Given that many of the sought-after multifunctional capabilities (e.g., vertical takeoff or landing), forward/backward/sideward flight, hovering and supermaneuverability) are inherent to naturally occurring flapping modes of flight, this paper advances the integrity of mechanized flapping-wing flight.

Flapping-wing flight is attracting an increasing amount of international multidisciplinary interest. There is now a small but growing group of aeronautical engineers who are variously persuaded of the utility of reexamining flapping flight,[1-12] as well as a number of mathematicians, biologists, and zoologists who are focused on the general topic of animal flight energetics.[13-16] Twentieth-century builders of flapping-wing flight vehicles, both ornithopters and orthopters [an ornithopter is a flapping-wing aircraft that has arched wings shaped like those of a bird (ornithos), and an orthopter is a flapping-wing aircraft that has regular or straight wing surfaces (orthos)[17]], include Lippisch,[1] Brooks et al.,[2] and most recently DeLaurier and Harris,[3] who have built a model ornithopter [DeLaurier and Harris define an ornithopter as any aircraft that flies like a bird (i.e., with flapping wings), whether or not its wings are arched and birdlike] with a wing span of approximately 10 ft. Although DeLaurier and Harris' model[3] must be manually launched, once in the air, it is capable of sustained flight.

Central to the development of flapping-wing technology (FWT) is an understanding of the dynamics and kinematics of flapping wings, the aerodynamic and structural forces acting on such wings, together with the availability of a suitable exemplar by which a simulation may be corroborated. Given that flapping-wing flight is an extraordinarily successful form of locomotion in the natural world, insect flight offers a particularly powerful and heuristic model for the design of flapping-wing aircraft. Following Smith,[5] Smith et al.,[6] and Wilkin and Williams,[13] this paper details a simulation of the flapping wings of a tethered sphingid moth *Manduca sexta*.

Received Nov. 18, 1994; presented as Paper 95-0743 at the AIAA 33rd Aerospace Sciences Meeting, Reno, NV, Jan. 9–12, 1995; revision received Feb. 26, 1996; accepted for publication Feb. 26, 1996.

*Postdoctoral Researcher, School of Aeronautics and Astronautics, 1282 Grissom Hall. Member AIAA.

Dynamics and Kinematics of Flapping Wings

To model the dynamic effects of moth wings, the equations of motion of an articulated flexible body are developed using Newton's equations of motion in an appendage-host body configuration in an inertial frame of reference.

Definition and Interrelations of the Vector Bases

In considering the equations of motion of a linearly elastic structure $\mathcal{A}$ attached to a rigid base $\mathcal{B}$, it is assumed that the motion of $\mathcal{A}$ relative to the base $\mathcal{B}$, and the base motion, are arbitrary. As a flexible appendage $\mathcal{A}$ is treated as a collection of elastically interconnected rigid subbodies $\mathcal{A}_1, \ldots, \mathcal{A}_s, \ldots, \mathcal{A}_n$. Definition of the sets of coordinate vector bases is also required. These bases are 1) the inertial axes $\{\boldsymbol{i}\}$, 2) the body-fixed axes $\{\boldsymbol{b}\}$, and 3) the wing axes $\{\boldsymbol{a}\}$ (see Fig. 1). Body $\mathcal{A}_s$ is a portion of appendage $\mathcal{A}$; $\boldsymbol{r}^s$ is the mass center vector of body $\mathcal{A}_s$, and O_i is a point fixed in inertial space. The inertial position vector $\boldsymbol{r}^s$ may be written as

$$\boldsymbol{r}^s = \boldsymbol{r}^x + \boldsymbol{r}^c + \boldsymbol{r}^r + \boldsymbol{r}^p + \boldsymbol{r}^d \tag{1}$$

where $\boldsymbol{r}^x$ is the inertial position vector from a point O_i to the body $\mathcal{B}$ mass center CM; $\boldsymbol{r}^c$ is the vector from CM to the point O_b fixed to body $\mathcal{B}$ and coincident with the CM when $\mathcal{B}$ is in some nominal undeformed configuration; $\boldsymbol{r}^r$ is the vector from O_b to a point O_a fixed in $\mathcal{B}$ on the interface between $\mathcal{A}$ and $\mathcal{B}$; $\boldsymbol{r}^p$ is the vector from O_a to the point P_s, occupied by $\boldsymbol{r}^s$ when $\mathcal{A}$ is undeformed; and $\boldsymbol{r}^d$ defines the translational deformation of the appendage at point P_s.

The vectors [in Eq. (1)] are not all expressed conveniently in any one vector basis. Vector $\boldsymbol{r}^x$ defines the vehicle trajectory that may be known in terms of an inertial reference. It is thus desirable to

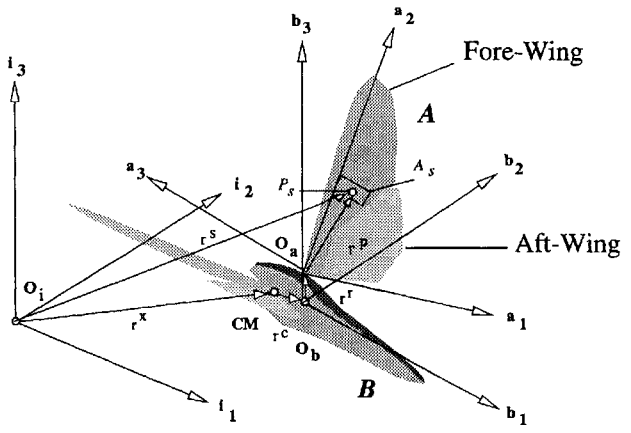

Fig. 1 Position vectors and coordinate bases definitions.

express $\boldsymbol{r}^x$ in terms of an inertially fixed basis $\boldsymbol{i}_1, \boldsymbol{i}_2, \boldsymbol{i}_3$. Vectors $\boldsymbol{r}^r$ and $\boldsymbol{r}^p$, on the other hand, are fixed in the reference frames in which the set of dextral orthogonal unit vectors $\boldsymbol{b}_1, \boldsymbol{b}_2, \boldsymbol{b}_3$ and $\boldsymbol{a}_1, \boldsymbol{a}_2, \boldsymbol{a}_3$ are embedded, respectively, and so they are most conveniently expressed in their own natural vector basis. The unit vectors $\boldsymbol{b}_1, \boldsymbol{b}_2, \boldsymbol{b}_3$ are fixed in the body $\mathcal{B}$, and a similar set $\boldsymbol{a}_1, \boldsymbol{a}_2, \boldsymbol{a}_3$ is fixed in the reference established by $\mathcal{A}$, before deformation (i.e., fixed in that portion of $\mathcal{A}$ contiguous to the rigid body $\mathcal{B}$). When $\mathcal{A}$ can rotate relative to $\mathcal{B}$, the transformation matrix relating these vector bases will vary with time. The direction cosine matrix T_{ib}, relating body $\mathcal{B}$ to the inertially fixed vector basis may be given by $\{\boldsymbol{i}\} = T_{ib}\{\boldsymbol{b}\}$, and the direction cosine matrix relating the $\{\boldsymbol{a}\}$ and $\{\boldsymbol{b}\}$ bases is given by $\{\boldsymbol{a}\} = T_{ab}\{\boldsymbol{b}\}$.

In terms of Euler angles the relationship between the $\{\boldsymbol{b}\}$ and $\{\boldsymbol{a}\}$ bases is given by the Euler 1–2–3, $(\psi\ \theta\ \phi)$ transformation

$$T_{ab} = \begin{bmatrix} \cos\theta\cos\psi & \cos\theta\sin\psi & -\sin\theta \\ \sin\phi\sin\theta\cos\psi - \cos\phi\sin\psi & \sin\phi\sin\theta\sin\psi + \cos\phi\cos\psi & \sin\phi\cos\theta \\ \cos\phi\sin\theta\cos\psi + \sin\phi\sin\psi & \cos\phi\sin\theta\sin\psi - \sin\phi\cos\psi & \cos\phi\cos\theta \end{bmatrix} \tag{2}$$

and $T_{ab} = (T_{ba})^{-1} = (T_{ba})^T$. In terms of Euler angles, a similar relationship between the $\{\boldsymbol{i}\}$ and $\{\boldsymbol{b}\}$ bases is given by the Euler 1–2–3, $(\Psi\ \Theta\ \Phi)$ transformation $T_{bi} = T_{bi}(\Psi, \Theta, \Phi)$.

Kinematic Relationships

The kinematic relationship between the Euler angle rates ${}^b_e\omega^a$ and the relative angular rotation rates ${}^b\omega^a$ between the $\{\boldsymbol{a}\}$ and the $\{\boldsymbol{b}\}$ axis systems is given by ${}^b_e\omega^a = T_{e\omega_a}\,{}^b\omega^a_a$, where ${}^b_e\omega^a = [\dot\phi\ \ \dot\theta\ \ \dot\psi\ ]^T$, ${}^b\omega^a = [p_a\ \ q_a\ \ r_a]^T$, and

$$T_{e\omega_a} = \begin{bmatrix} 1 & \sin\phi\tan\theta & \cos\phi\tan\theta \\ 0 & \cos\phi & -\sin\phi \\ 0 & \sin\phi\sec\theta & \cos\phi\sec\theta \end{bmatrix} \tag{3}$$

Also, ${}^b\omega^a_a = T_{\omega_a e}\,{}^b_e\omega^a$, where

$$T_{\omega_a e} = \begin{bmatrix} 1 & 0 & -\sin\theta \\ 0 & \cos\phi & \sin\phi\cos\theta \\ 0 & -\sin\phi & \cos\phi\cos\theta \end{bmatrix} = (T_{e\omega_a})^{-1} \tag{4}$$

Similarly, one may define for the relative angular rotation rates between the $\{\boldsymbol{i}\}$ and the $\{\boldsymbol{b}\}$ axis systems ${}^i_e\omega^b = T_{e\omega_b}\,{}^i\omega^b_b$, where ${}^i_e\omega^b = [\dot\Phi\ \ \dot\Theta\ \ \dot\Psi]^T$, ${}^i\omega^b_b = [p_b\ \ q_b\ \ r_b]^T$, and $T_{e\omega_b} = T_{e\omega_b}(\Psi, \Theta, \Phi)$ has the same form as $T_{e\omega_a}$.

Equations of Motion

Each vector in Eq. (1) may be defined in terms of its appropriate vector bases and corresponding coordinate vectors as follows:

$$\boldsymbol{r}^x = \{\boldsymbol{i}_1, \boldsymbol{i}_2, \boldsymbol{i}_3\}\begin{bmatrix} r^x_1 & r^x_2 & r^x_3 \end{bmatrix}^T = \{\boldsymbol{i}\}^T r^x_i \tag{5}$$

Similarly, $\boldsymbol{r}^c = \{\boldsymbol{b}\}^T r^c_b$, $\boldsymbol{r}^r = \{\boldsymbol{b}\}^T r^r_b$, $\boldsymbol{r}^p = \{\boldsymbol{a}\}^T r^p_a$, and $\boldsymbol{r}^d = \{\boldsymbol{a}\}^T r^d_a$. Newton's second law provides

$$\boldsymbol{F}^s = m_s(\ddot{\boldsymbol{r}}^s) \tag{6}$$

where $\boldsymbol{F}^s$ is the resultant force applied to $\mathcal{A}_s$, m_s is the mass of $\mathcal{A}_s$, $\boldsymbol{r}^s$ is the position vector from O_i to P_s, and each dot over a vector denotes time differentiation in an inertial frame of reference.

Equations (1) and (6) may be combined as

$$\boldsymbol{F}^s = m_s\left[\frac{{}^i\mathrm{d}^2}{\mathrm{d}t^2}\boldsymbol{r}^x + \frac{{}^i\mathrm{d}^2}{\mathrm{d}t^2}(\boldsymbol{r}^c + \boldsymbol{r}^r) + \frac{{}^i\mathrm{d}^2}{\mathrm{d}t^2}(\boldsymbol{r}^p + \boldsymbol{r}^d)\right] \tag{7}$$

By repeated use of the identity $({}^{f_1}\mathrm{d}/\mathrm{d}t)\boldsymbol{V} = ({}^{f_2}\mathrm{d}/\mathrm{d}t)\boldsymbol{V} + {}^{f_1}\omega^{f_2} \times \boldsymbol{V}$ (where $\boldsymbol{V}$ is any vector, ${}^{f_1}\omega^{f_2}$ is the angular velocity of any reference frame f_2 relative to any other reference frame f_1, t is time, and the superscript preceding the derivative operator denotes the reference frame of differentiation) and using the matrix equivalent of a vector cross product, Eq. (7) reduces (in the $\{\boldsymbol{a}\}$ basis) to

$$\begin{aligned} F^s = m^s\{&T_{ab}\big[T_{bi}\ddot r^x_i + \ddot r^c_b + 2(\widetilde{{}^i\omega^b_b})\dot r^c_b + (\widetilde{{}^i\omega^b_b})(\widetilde{{}^i\omega^b_b})(r^c_b + r^s_b) \\ &- (\widetilde{r^c_b + r^s_b})\,{}^i\dot\omega^b_b\big] - (\widetilde{r^p_a + r^a_a})({}^b\dot\omega^a_a + T_{ab}\,{}^i\dot\omega^b_b) \\ &+ \big[(\widetilde{T_{ab}\,{}^i\omega^b_b})(\widetilde{T_{ab}\,{}^i\omega^b_b}) + 2(\widetilde{T_{ab}\,{}^i\omega^b_b}) \\ &+ (\widetilde{{}^b\omega^a_a})(\widetilde{{}^b\omega^a_a})\big](r^p_a + r^d_a) + 2\big[\widetilde{{}^b\omega^a_a}(\widetilde{T_{ab}\,{}^i\omega^b_b})\big]\dot r^d_a + \ddot r^d_a\} \end{aligned} \tag{8}$$

where a is the reference frame of body $\mathcal{A}$ (basis $\{\boldsymbol{a}\}$), b is the reference frame of body $\mathcal{B}$ (basis $\{\boldsymbol{b}\}$), ${}^i\omega^b$ is the inertial angular velocity of basis $\{\boldsymbol{b}\}$ with respect to basis $\{\boldsymbol{i}\}$, ${}^i\omega^b = \{p_b\ \ q_b\ \ r_b\}^T$, ${}^b\omega^a$ is the inertial angular velocity of basis $\{\boldsymbol{a}\}$ with respect to basis $\{\boldsymbol{b}\}$, ${}^b\omega^a = \{p_a\ \ q_a\ \ r_a\}^T$, $\boldsymbol{r}^r$ is assumed to be constant, the time derivative of $\boldsymbol{r}^p$ in basis $\{\boldsymbol{a}\}$ is zero, $\{\boldsymbol{b}\}^T = \{\boldsymbol{a}\}^T T_{ab}$, and $\{\boldsymbol{i}\}^T = \{\boldsymbol{b}\}^T T_{bi} = \{\boldsymbol{a}\}^T T_{ab} T_{bi}$. (For two arbitrary vectors $\boldsymbol{V}$ and $\boldsymbol{W}$, expressed in terms of an arbitrary vector basis $\{\boldsymbol{e}\}$, the vector cross product may be written as $\boldsymbol{V} \times \boldsymbol{W} = \{\boldsymbol{e}\}^T V \times \{\boldsymbol{e}\}^T W = \{\boldsymbol{e}\}^T \tilde V W$, where $V = [V_1\ \ V_2\ \ V_3]^T$, $W = [W_1\ \ W_2\ \ W_3]^T$, and

$$\tilde V = \begin{bmatrix} 0 & -V_3 & V_2 \\ V_3 & 0 & -V_1 \\ -V_2 & V_1 & 0 \end{bmatrix}$$

Thus the matrix identity $\tilde V W = -\tilde W V$ follows from the vector identity $\boldsymbol{V} \times \boldsymbol{W} = -\boldsymbol{W} \times \boldsymbol{V}$. The tilde operator ~ over a 3×1 matrix represents the corresponding skew-symmetric 3×3 matrix. Note the identity $\tilde V^T = -\tilde V$.)

Equation (8) is the equation of motion of a representative portion of an articulated flexible body in an appendage-host body configuration in an inertial frame of reference. The force F^s includes terms that result from interactions with the other subbodies of $\mathcal{A}$ (which in this study are considered to be linearly elastic forces), as well as terms that result from any external aerodynamic forces. Equation (8) may be assembled for the whole collection of subbodies $\mathcal{A}_s$. Rearranging the equations such that the focus is on the appendage deformations, the resulting matrix equation (in the coordinate basis $\{\boldsymbol{a}\}$) for all subbodies s is given by

$$\begin{aligned} &M'\ddot q + (D' + G)\dot q + (K' + A')\boldsymbol{q} = \boldsymbol{L}(\ddot x, \dot x, x) \\ &\quad = \boldsymbol{M}(\ddot x, \dot x, x) + \boldsymbol{A}(\ddot x, \dot x, x) \end{aligned} \tag{9}$$

where D' and K' are symmetric matrices and G' and A' are skew-symmetric matrices; $\boldsymbol{q}$ is a vector of the deformations of the wing elements, where $\boldsymbol{q} = [r^d_1\ \ r^d_2\ \ r^d_3]$; x is the global position of a wing element given by $x(\phi, \theta, \psi, r^p)$; $\boldsymbol{L}$ is the vector of externally applied forces as a result of the motion of the wing; $\boldsymbol{M}$ is the vector of inertial forces on the wing; $\boldsymbol{A}$ is the vector of aerodynamic forces on the wing; M' is the mass matrix; D' is the damping matrix; G is the coriolis matrix; $A' + K'$ accommodate geometric stiffness effects in the wing structure as well as the symmetric stiffness matrix K; ϕ, θ, and ψ are the Euler angles (flap, pitch, and azimuth/lead-lag angies, respectively) of the experimentally derived wing trajectory taken at the wing root; and r^p is the position vector of a wing element in the wing coordinate system $\{\boldsymbol{a}\}$. Relevant coefficient matrices (M' and K) and the vectors of aerodynamic forces A and inertial forces M for the simulation are determined in due course.

Unsteady Aerodynamic Panel Method

Current research establishes that flapping flight is an aeroelastic, dynamic phenomenon characterized by rapid reversals in stroke direction and in wing rotation that result in gross movements of and

between lifting surfaces and produce the necessary aerodynamic forces for flight in a highly efficient manner. Prevailing methods establish that any attempt to model the aerodynamic forces on flapping wings must both accommodate vortex effects in a detailed manner (given the extreme operational environment of large wing displacements) and include wing flexibility effects (both spanwise and chordwise). Moreover, to correlate better the in-flight measurements of metabolic rates with predictions of power expenditure, both the aerodynamic and structural (morphological) characteristics must be modeled.

There are six predominant methods used to determine the aerodynamic forces on flapping wings: momentum method,[8,18] blade element method,[8,13] hybrid momentum (or vortex) method,[14] two-dimensional thin airfoil method,[19] lifting-line method,[9,10] and a lifting-surface (or vortex lattice) method.[11] The problem with existing methods is that although some can accommodate vortex effects in a detailed manner and others can include spanwise wing-flexibility effects, not one of the methods is capable of both.[5,6] Moreover, studies using prevailing methods that attempt to correlate the in-flight measurements of metabolic rates with predictions of power expenditure do not provide the necessary comprehensive analysis of the aerodynamic, inertial, and structural forces involved.

The aerodynamic flows of the sphingid moth are for Reynolds number Re ($Re = cU/\nu$ where c is a nominal chord length; U is based on the flapping frequency, a nominal radius, and the freestream velocity; and ν is the kinematic viscosity of air) on the order of 10^4 and involve large-amplitude wing strokes. Reduced frequencies k ($k = \pi nc/U$, where n is the wing-beat frequency and c and U are as defined earlier) are on the order of 0.2 or more. The Reynolds number range suggests that the airflows are inertially dominated, and as such, viscous effects should not be directly important in most of the flowfield. Viscous effects are thus confined to regions near the body, the wing, and the wake that is shed behind the body or the wing. In contrast to high-speed flows of aeronautical interest (Reynolds numbers on the order of 10^7), the flows should be mostly laminar, and so uncertainties of turbulence modeling should not arise. In the light of these parameters, this project implements a type of lifting surface method known as an unsteady aerodynamic panel method.[5-7,20,21] The panel method accommodates the detailing of the trailing wake, includes dynamic effects, and facilitates an accounting of flexibility and interference effects necessary for detailed design loads analyses.

To simulate the aerodynamic flow, an inviscid, three-dimensional, potential, unsteady solver is constructed that amounts to solving Laplace's equation in space, with impermeability conditions imposed on the moving wing surfaces. (Although viscous effects are not considered in this study, it is possible to account for such effects using a boundary-layer solution that is matched to the potential flow solution.) A current panel method computer program that meets the requirements of solving Laplace's equation and details the wake is PMARC.[20,21] Although PMARC does not include dynamic effects, it can be modified to do so by incorporating the temporal dependency through the boundary conditions that are developed in the kinematic relations. For further discussion of the potential flow model, including its theoretical derivation, model discretization, and computation of velocity components, pressures, and loads, see Refs. 5, 6, and 20.

The panel method develops the aerodynamic forces at the centroids of the aerodynamic panels. For the equations of motion [see Eq. (9)] to be internally consistent, these forces need to be transferred to the structural control points. This is undertaken by a load transformation matrix T_c^T, such that the aerodynamic forces at the structural node points are given by $T_c^T \Delta F_{ak}$.

Structural Considerations

DeLaurier[4] utilizes a simple beam model that specifies the spanwise torsional and bending stiffness distribution of the spars. Although DeLaurier's model facilitates the assessment of general design parameters, it does not facilitate a detailed design loads analysis for low-aspect-ratio wings. Needless to say, for design purposes, both the structural and inertial forces are best calculated in a distributed manner. A finite element formulation, therefore, better represents the complicated structure of an insect wing and also provides a basis by which interaction with the associated aerodynamic forces can be accommodated.

Table 1 Combined wing node-point data

	Degree of freedom						Coordinates	
Node	X	Y	Z	θ_x	θ_y	θ_z	X, m	Y, m
1	0	0	0	0	0	0	0.0002633	0.000000
2	0	0	0	0	0	0	0.0015681	0.000000
3	0	0	1	2	3	0	0.0039161	0.0216157
4	0	0	4	5	6	0	−0.0015851	0.0277801
5	0	0	7	8	9	0	−0.0023471	0.0401145
6	0	0	10	11	12	0	0.0000016	0.0561941
7	0	0	13	14	15	0	0.0036552	0.0539758
8	0	0	16	17	18	0	0.0071783	0.0512356
9	0	0	19	20	21	0	0.0017242	0.0247859
10	0	0	22	23	24	0	0.0102052	0.0454265
11	0	0	25	26	27	0	0.0120320	0.0411205
12	0	0	28	29	30	0	0.0035516	0.0191492
13	0	0	31	32	33	0	0.0102257	0.0305211
14	0	0	34	35	36	0	0.0136240	0.0363976
15	0	0	37	38	39	0	0.0030548	0.0142152
16	0	0	40	41	42	0	0.0089266	0.0233492
17	0	0	43	44	45	0	0.0145374	0.0327440
18	0	0	0	0	0	0	0.0042292	0.000000
19	0	0	46	47	48	0	0.0099705	0.0203480
20	0	0	49	50	51	0	0.0159727	0.0290905
21	0	0	0	0	0	0	0.0065665	0.000000
22	0	0	52	53	54	0	0.0099705	0.0178688
23	0	0	55	56	57	0	0.0174335	0.0262757
24	0	0	58	59	60	0	−0.0006732	0.0161340
25	0	0	61	62	63	0	−0.0012855	0.0227466
26	0	0	64	65	66	0	0.0064292	0.0122154
27	0	0	67	68	69	0	0.0074770	0.0106444
28	0	0	70	71	72	0	0.0125796	0.0200141
29	0	0	73	74	75	0	0.0124603	0.0239292
30	0	0	76	77	78	0	0.0111195	0.0267224
31	0	0	79	80	81	0	0.0089967	0.0336494
32	0	0	82	83	84	0	0.0064270	0.0376716
33	0	0	85	86	87	0	0.0040808	0.0424758
34	0	0	88	89	90	0	0.0012876	0.0482856
35	0	0	91	92	93	0	−0.0024862	0.0504465
36	0	0	94	95	96	0	0.00128762	0.0339846
37	0	0	97	98	99	0	0.00385733	0.0302976
38	0	0	100	101	102	0	0.00665049	0.0278396
39	0	0	103	104	105	0	0.00765602	0.0257168
40	0	0	106	107	108	0	0.00090839	0.0211357
41	0	0	109	110	111	0	0.00113184	0.0152142
42	0	0	0	0	0	0	0.0008000	0.000000
43	0	0	0	0	0	0	0.0081285	0.000000
44	0	0	112	113	114	0	0.0120979	0.0075855
45	0	0	115	116	117	0	0.0094291	0.0091347
46	0	0	0	0	0	0	0.0101450	0.000000
47	0	0	0	0	0	0	0.0111863	0.000000
48	0	0	118	119	120	0	0.0201930	0.0023139
49	0	0	121	122	123	0	0.0151164	0.0026394
50	0	0	124	125	126	0	0.0216248	0.0044617
51	0	0	127	128	129	0	0.0166534	0.0068570
52	0	0	130	131	132	0	0.0255298	0.0098635
53	0	0	133	134	135	0	0.0182023	0.0106314
54	0	0	136	137	138	0	0.0243974	0.0136381
55	0	0	139	140	141	0	0.0173562	0.0131046
56	0	0	142	143	144	0	0.0236295	0.0163063
57	0	0	145	146	147	0	0.0163153	0.0154601
58	0	0	148	149	150	0	0.0221199	0.0206744
59	0	0	151	152	153	0	0.0147535	0.0183233
60	0	0	154	155	156	0	0.0206754	0.0235555
61	0	0	157	158	159	0	0.0136471	0.0198722
62	0	0	160	161	162	0	0.0197123	0.0256249
63	0	0	0	0	0	0	0.0073604	0.000000
64	0	0	163	164	165	0	0.0155861	0.0013504

Finite Element Formulation of a Sphingid Moth Wing

To develop mass and stiffness matrices of a moth wing, discretization of the fore and aft wing venation is necessary. To simplify the wing model, the fore and aft wings are combined as one wing. Figure 2 illustrates the arrangement of the structural nodal points. Table 1 lists the nodal points, the degrees of freedom, and the coordinates of the combined wing structure.

Table 2 Combined wing structural data

Elastic modulus, N/m^2	E	10^{10}
Density, kg/m^3	ρ	1200
Mass of wing, mg	M_w	39.743 (cf. 36.935) (Ref. 15)
Center of mass, m	cg	2.36×10^{-2} (cf. 2.3673×10^{-2}) (Ref. 15)
Radius of gyration, m	r_g	2.696×10^{-2} (cf. 2.8368×10^{-2}) (Ref. 15)
Radius of wing, m	r_w	5.619×10^{-2}
Wing thickness	t	Varies linearly from 55 to 33 μm root to tip
Wing area, m^2	S	0.0009828
Cross-sectional area of leading-edge veins, m^2 (beam type 1)	A_1	1225×10^{-11}
Cross-sectional area of all other veins, m^2 (beam type 2)	A_2	4084×10^{-12}
Polar moment of area of leading-edge veins, m^4 (beam type 1)	I_1	8.625×10^{-17}
Polar moment of area of all other veins, m^4 (beam type 2)	I_2	17.255×10^{-18}
Inner radius of veins, μm	r_i	60
Outer radius of veins, μm	r_o	70
Modal frequencies, Hz		
First bending		144
First torsion		474
Second bending		731
Second torsion		961

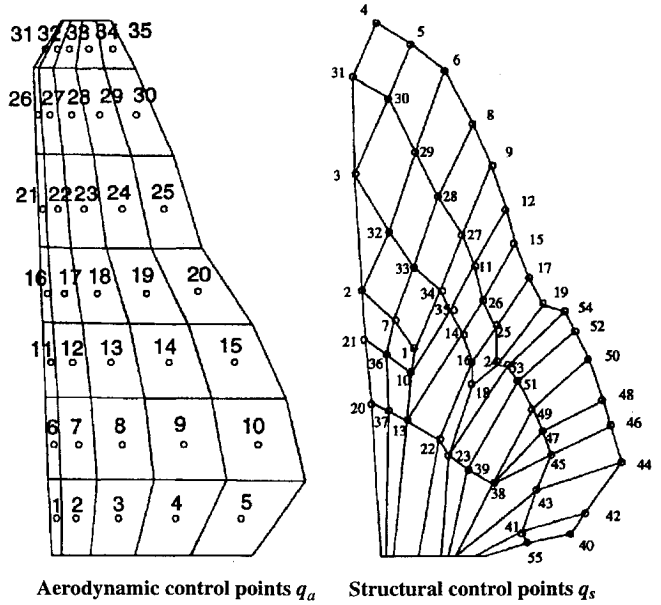

Fig. 2 Combined wing: aerodynamic and structural control point arrangements. The aerodynamic control points of corresponding upper and lower wing panel surfaces are combined as one in a NACA 0001 airfoil section (left).

Using the finite element program SAP IV (Ref. 22), the veins are modeled as three-dimensional tubular beam elements of varying thickness. The wing surface is modeled as quadrilateral (or triangular) orthotropic plane stress membranes that are also of varying thickness (see Fig. 2 and Table 2). The thickness is distributed so as to correspond with published values of wing mass, center of mass, and radius of gyration for a sphingid moth wing.[15] These properties of the wing, together with Young's modulus and material density,[23] are given in Table 2.

Because of the general absence of experimental data (except for some investigations of locust wings[16]), a modal analysis of the combined wing structure is undertaken so that a correlation of the distribution of mass and stiffness eventually may be achieved.

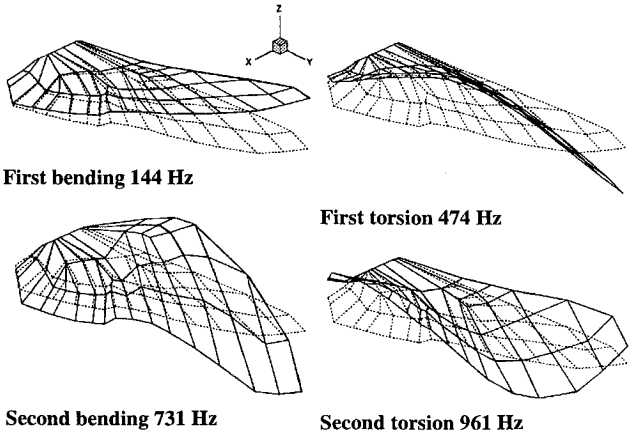

Fig. 3 Combined wing: first four mode shapes.

(Comparisons of the mechanical properties of insect wings with those of more regularly folded and tubularly reinforced beams has been investigated by Rees.[23] He concludes that the bending stiffness of typical insect wings is increased by a factor of approximately 300 because of the corrugations, and the buckling failure of the wings is reduced by the placement of the tubes at the folds. This factor is included in the present analysis.) Figure 3 details the first four resulting mode shapes and frequencies of the combined wing model. The mechanization of the equations of motion for the deformation of a flexible appendage undergoing arbitrarily large displacements in a fluid medium requires the synthesis of the foregoing dynamic, kinematic, aerodynamic, and structural preliminaries.

Equations of Motion for the Deflection of a Tethered Moth Wing

If the acceleration and structural damping forces, as well as geometric stiffness effects as a result of the deformation of the wing, are ignored (this is justified under the assumption that the wing deformation is small), the deformation of the wing as a result of the imposed motion of the wing may be represented as

$$q = F[M(\ddot{x}, \dot{x}, x, q) + A(\ddot{x}, \dot{x}, x, q)] \tag{10}$$

where $F = K^{-1}$ is the flexibility matrix of the wing; $M(\ddot{x}, \dot{x}, x, q)$ is given by $[M^1\ M^2\ \cdots\ M^s\ \cdots]^T$, where M^s is the inertial force acting at the structural node s; $A(\ddot{x}, \dot{x}, x, q)$ is given by $[A^1\ A^2\ \cdots\ A^s\ \cdots]^T$, where A^s is the aerodynamic force acting at the structural node s; and $q = [r_1^d\ r_2^d\ r_3^d]$ is the deformation of the wing at the structural node s. If the variables $\ddot{r}_i^x$, $\ddot{r}_b^c$, $\dot{r}_b^c$, $\dot{r}_a^d$, $\ddot{r}_a^d$, ${}^i\omega_b^b$, and ${}^i\dot{\omega}_b^b$ are assumed to be zero (as in the case of a tethered flexible body), then from Eq. (8),

$$M^s = m^s\{[\widetilde{{}^b\dot{\omega}_a^a} + (\widetilde{{}^b\omega_a^a})(\widetilde{{}^b\omega_a^a})](r_a^p + r_a^d)\} \tag{11}$$

The deformation q is iterated at each time step, and as such the aerodynamic potential influence coefficient matrices are also recalculated, taking into account the deformed wing. The iteration process is continued until the resultant increment in aerodynamic force between time steps is within a minimal percentage. In this study the in-plane deformations of the wing are ignored. The term A^s is the aerodynamic force acting at the structural node point s and is given by

$$A^s = T_c^T A^a \tag{12}$$

where T_c^T is a load transformation matrix that relates A^a to A^s (to be developed in the next section), and A^a is the aerodynamic force at the aerodynamic control points a (see Fig. 2 for the arrangement of the structural and aerodynamic control points).

Development of the Aerodynamic Load Transformation Matrix

The control points in the aerodynamic and structural models do not coincide because of the use of different discretization procedures. It is necessary to represent equivalent airloads at the structural

control points and the displacements of the structural control points at the aerodynamic paneling coordinates. Various schemes, including the infinite-surface spline of Harder and Desmarais,[24] have been developed to obtain the necessary transformations. Appa[25] notes that experience with the infinite-surface spline indicates that extrapolation to the edges of the planform (of a wing) from the interior structural grid points is not always reliable. Following Appa,[25] a finite surface spline method is developed that transfers pressure or airloads from aerodynamic grid points to structural grid points and updates the aerodynamic configuration given the structural deformation.

The finite surface spline method uses uniform quadrilateral or triangular plate elements to develop a pseudostructural plate that is constrained to pass through a set of given data points (e.g., structural displacements). A mapping matrix relating these displacements and any other on the plate (e.g., aerodynamic control points) is then derived, providing a general two-dimensional interpolation scheme between these two sets of points. The relationship between the constrained structural displacement points q_s and any general displacement q of the pseudostructure may be given by $q_s = \Psi_s q$, and the relationship between the aerodynamic control points q_{ac} and q may be represented as $q_{ac} = \Psi_{ac} q$. The relationship between the aerodynamic paneling points q_{ap} and q may be represented as $q_{ap} = \Psi_{ap} q$. Since the pseudostructure is required to pass through the displacements q_s, using the method of penalty constraints the equilibrium state of the structure is given by $\left[K_{ps} + \alpha_{ps}\Psi_s^T \Psi_s\right] q = \alpha_{ps}\Psi_s^T q_s$, where K_{ps} is the free-free stiffness of the pseudostructure and α_{ps} is a constant. The relationship between the displacements at the aerodynamic control points and the structural control points may be represented, therefore, as $q_{ac} = T_c q_s$, where

$$T_c = \Psi_{ac}\left[\alpha_{ps}^{-1} K_{ps} + \Psi_s^T \Psi_s\right]^{-1} \Psi_s^T \tag{13}$$

Similarly, the transformation matrix between the aerodynamic paneling coordinates and the structural control points may be represented as $q_{ap} = T_p q_s$, where

$$T_p = \Psi_{ap}\left[\alpha_{ps}^{-1} K_{ps} + \Psi_s^T \Psi_s\right]^{-1} \Psi_s^T \tag{14}$$

The aerodynamic load transformation (from the principle of virtual work) can then be given by

$$A^s = T_c^T A^a \tag{15}$$

where A^a is the set of aerodynamic forces acting at the aerodynamic control points q_{ac}, A^s is the set of kinematically consistent aerodynamic forces acting at the structural control points q_s, and T_c^T is the aerodynamic load transformation matrix.

Development of the Boundary Conditions

For the puposes of consistency, the experimental wings-to-planes angles are converted to Euler angle form. Defining the line joining the root R and the tip T of the wing to be the RT axis, the angle between the projection of the RT axis on the $\boldsymbol{b}_3\boldsymbol{b}_2$ plane and the $\boldsymbol{b}_2$ axis is v. The angle between the projection of the RT axis on the $\boldsymbol{b}_1\boldsymbol{b}_2$ plane and the $\boldsymbol{b}_2$ axis is h.

The angle h serves as a measure of the Euler angle ψ. From geometric considerations, $\theta_{\text{exp}} = \tan^{-1}(\tan v \cos h)$ and serves as a measure of the Euler angle ϕ. The rotation of the wing about the RT axis is obtained from measurements of the projected chord of the wing on the $X-Y$ plane and the actual wing chord at different wing sections. This rotation angle serves as a measure of the Euler angle θ at the root of the wing and also as a measure of the twist of the wing along its span. Thus the wing-angles-to-planes data are converted into the Euler angles ψ, ϕ, and θ. The derivatives of these angles with respect to time may be developed numerically. Using the aforementioned kinematic relationships, the angular velocities p_a, q_a, and r_a are developed. The determination of the normal kinematic velocity on the wing surfaces and hence the boundary conditions then follows. A plot of the derived Euler angles as a function of the wing-beat cycle is shown in Fig. 4. (The motion of the wing is described using the terms supination and pronation, downstroke and upstroke, forwardstroke and backstroke, in correspondence with the wing motion between the extreme values of the Euler angles Θ, Φ, and Ψ, respectively. These terms are used in Fig. 4 and all relevant subsequent figures.)

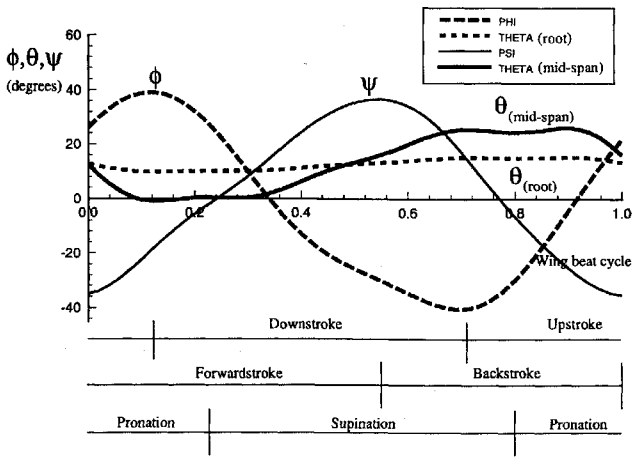

Fig. 4 Derived wing trajectory Euler angles. ——, psi and ——, theta (mid-span)

Validation

The validity of the code was established by comparing data generated by the code with data developed by Katz and Plotkin[20] for the vertical oscillation (plunging) of an inclined flat plate and the pitch oscillation of a 0012 section wing. The high correlations obtained in both test cases proved the simulation code to be valid.

Simulation

Having established the validity of the code, the in-flight forces on the wings of a tethered sphingid moth *Manduca sexta* are then simulated. First, the modeling assumptions concerning the structural and aerodynamic properties of the wings are delineated. Second, the trajectory of the wings (including their flexure or twisting) is derived from experimentally determined wings-to-planes angular data because such a trajectory illuminates any aerodynamic modeling deficiencies. The trajectory is then used to forcibly simulate the flapping motion of the wings. Finally, to establish the adequacy of the structural model, an investigation is conducted into the autonomous or free flexing of the wing by forcing the motion of the wing from the root only. A distinction is thus made between a forced wing condition and a free wing condition based on whether the trajectory of the wing includes both the control of the root angular motion and the wing twist or just the root angular motion. Aerodynamic forces and work output for both studies are then compared with each other and the experimental data of Wilkin and Williams. [Wilkin and Williams provide the wind-tunnel wind velocity (3.36 m/s), wing-beat frequency (22.2 Hz), and derived aerodynamic vertical and horizontal forces acting on the wings of a tethered sphingid moth. The latter forces are derived by subtracting estimates of the inertial forces from measured data that include both the aerodynamic and inertial forces. Wilkin and Williams[13] also assume the twist of the wing to vary linearly from the root to the tip.]

Modeling Assumptions: Forced- and Free-Wing Conditions

To model the aerodynamic forces of a tethered sphingid moth in both the forced- and the free-wing conditions, the following assumptions apply.

1) The fore and aft wings of the moth are combined as one (see Fig. 1).

2) Each combined wing is considered to be flexible with a symmetric NACA 0001 section (i.e., an arbitrarily very thin aerofoil).

3) The wing vortices are generated at the trailing edge only.

4) The rounded leading edges (the veins) of the wings and the corrugated profile of the wing surface inhibit leading-edge separation.[26]

5) Leading-edge suction is not included.

6) The wing is hinged by a universal joint at a root location.

7) The root chord is rigid.

8) The velocity of trailing-edge vortices are dependent on the kinematic velocity of, as well as the tangential fluid velocity relative to, the trailing-edge wing surface.

9) The wings act independently of each other.

10) The effect of the body is not included.

Experimental Aerodynamic Force and Work: Forced- and Free-Wing Conditions

Like Wilkin and Williams,[13] the experimentally determined aerodynamic forces are determined by subtracting estimates of the inertial forces from the measured forces. In this study the inertial forces are developed based on a finite element formulation, which allows for a more accurate representation of the mass distribution and more accurate kinematic analysis. The presently developed experimental aerodynamic forces and work are used as a basis for further comparison.

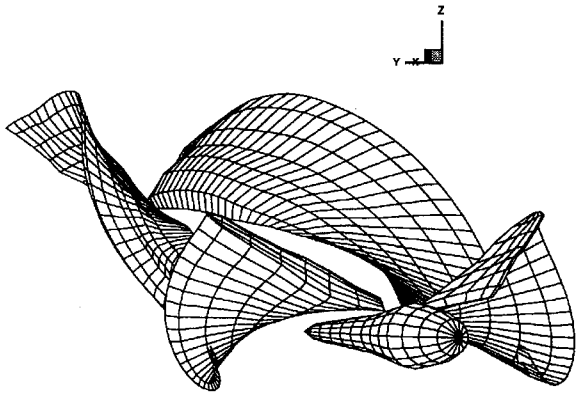

Fig. 5 Forced-wing: wake development after one wing beat cycle (front underside view).

Forced-Wing Condition with Wake: Assumptions and Results

A modeling assumption exclusive to the forced-wing condition is that the twist of the wing is assumed to vary linearly from the root to the tip. The trajectory of the wing (see Fig. 4) is derived using the boundary conditions previously outlined. A view of the wake developed over one cycle is shown in Fig. 5.

Figure 6 reveals that the predicted aerodynamic lift force in the downstroke/supination segment of the wing beat compares well with the experimental data, whereas the predicted aerodynamic lift force on the upstroke/pronation segment of the wing beat is in excess of the experimentally determined lift force. Figure 6 also reveals that the simulation thrust on the pronation segment of the wing beat is slightly lower (or higher in the case of drag) than the experimental result. On the supination segment of the wing beat, the situation is reversed, with the simulation thrust being slightly higher (or lower in the case of drag) than the experimental result.

Although the preceding aerodynamic force results are presented in vector component form, if they are presented in vector magnitude and direction form, an interesting phenomenon is discovered. Figure 7 shows a comparison between magnitudes of the resultant aerodynamic force and the experimental aerodynamic force, and Fig. 8 shows a comparison between the directions of the resultant aerodynamic force and the experimental aerodynamic force. The direction of the resultant aerodynamic force follows a switching

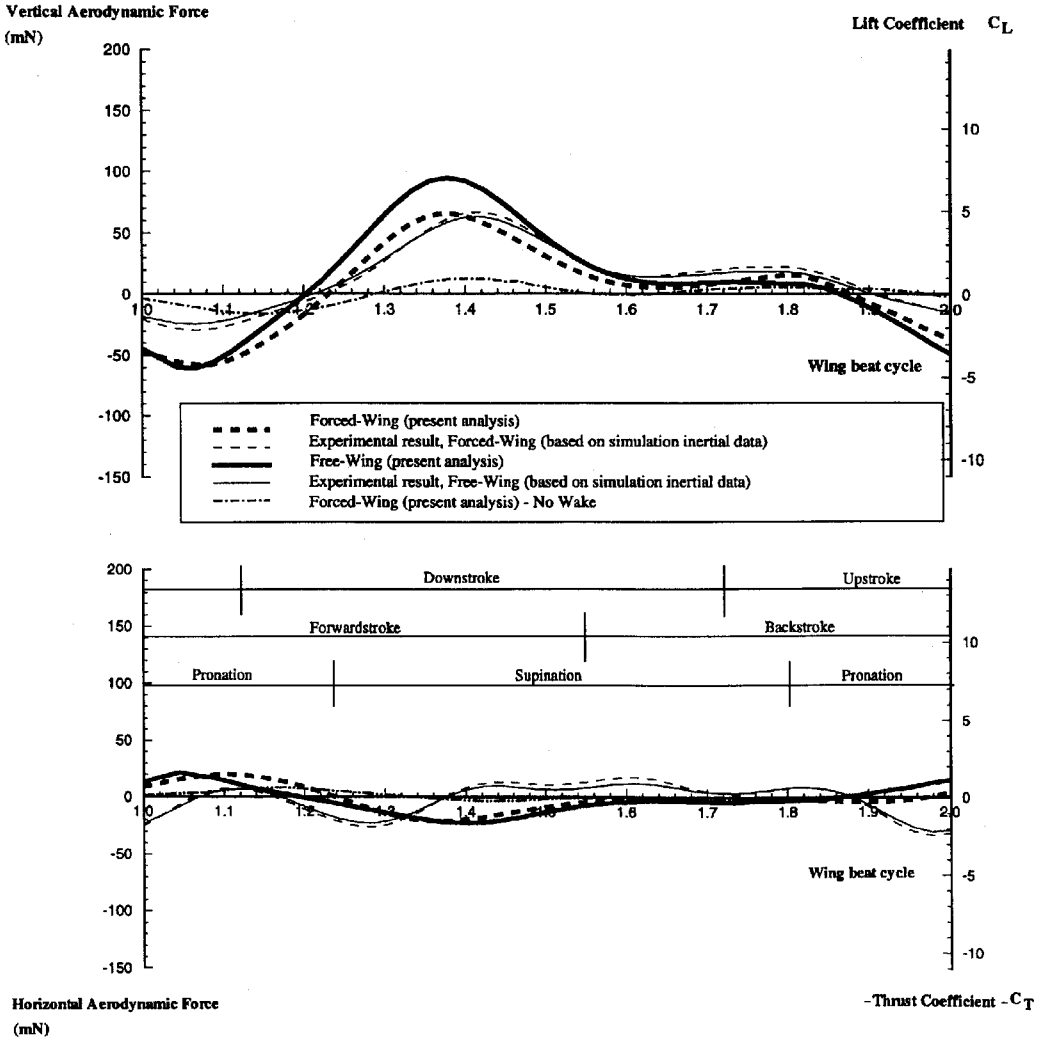

Fig. 6 Comparison between forced-wing, free-wing, and experimental vertical and horizontal aerodynamic forces over one wing beat cycle.

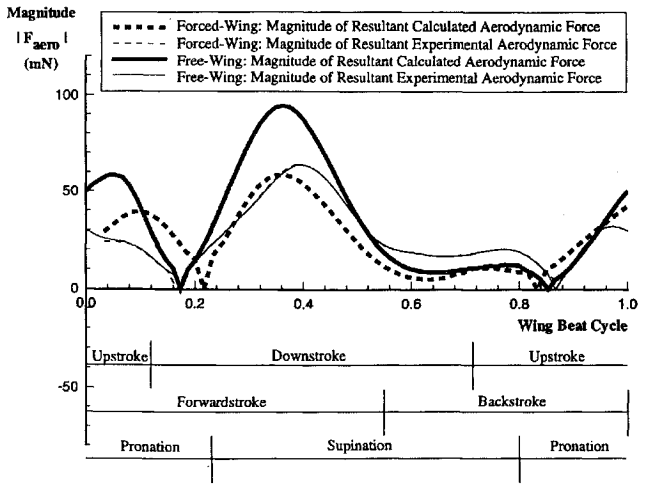

Fig. 7 Forced-wing and free-wing: comparison between magnitudes of resultant calculated and experimental aerodynamic forces.

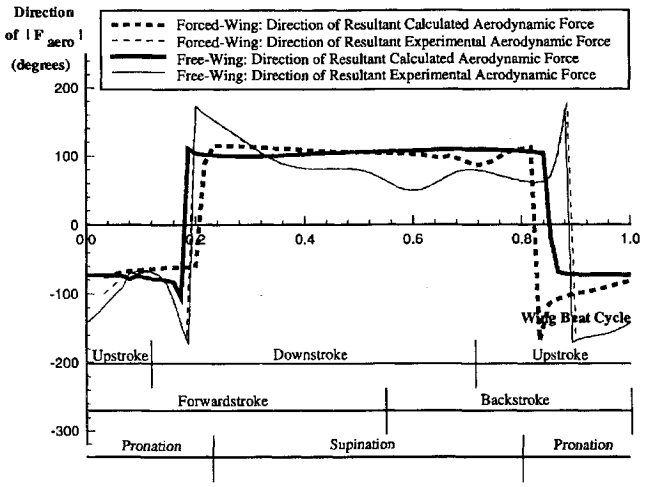

Fig. 8 Forced-wing and free-wing: comparison between directions of resultant calculated and experimental aerodynamic forces.

pattern that is coincident with the supination and pronation segments of the wing beat. That is, the direction of the aerodynamic force over each of the supination and pronation segments of the wing-beat cycle is a constant. These alternating directions also appear to be diametrically opposed to each other.

Free-Wing Condition with Wake: Assumptions and Results

To address the free or autonomous flexing of the moth wing and thereby illuminate flexibility effects, only the root motion is forced. The flexibility effects are taken into account by modeling the moth wing as a linearly elastic structure using finite elements.

Following Eq. (10), a modeling assumption exclusive to the free-wing condition is that if the acceleration and structural damping forces, as well as the geometric stiffness effects as a result of the deformation of the wing, are ignored, the deformation of the wing as a result of the imposed motion of the wing may be represented as $q = F[M(\ddot{x}, \dot{x}, x, q) + A(\ddot{x}, \dot{x}, x, q)]$. Moreover, the motion of the wing as a whole is allowed to be driven by the derived values of only the root wing pitch θ, flap ϕ, and azimuth (lead-lag) ψ Euler angles (see Fig. 4).

Given the disadvantages of DeLaurier's beam model as it pertains to low-aspect-ratio wings, a finite element model of the moth wing is constructed (see Fig. 2). The model enables flexibility and mass matrices to be determined. As stated earlier, the veins of the wings are treated as tubular beams of varying thickness, and the wing surfaces are modeled as quadrilateral (or triangular) membranes that are also of varying thicknesses with orthotropic properties. Table 2 summarizes the material properties of the wing, including Young's modulus, density, and skin thickness.[23]

The finite element model also determines the inertial properties of the wing. As discussed earlier, the wing mass is distributed so as to correspond with published values of wing mass, center of mass, and radius of gyration for the moth wing,[15] and Fig. 3 details the first four mode shapes of the current combined wing model. Since different discretization procedures are used to represent the aerodynamic and structural models, the control points in the two models do not coincide. It is thus necessary to represent equivalent airloads at the structural control points and the displacements of the structural control points at the aerodynamic paneling coordinates.

The free-wing results (see Figs. 6–8) generally follow those of the forced-wing analysis, although the differences with the experimental results tend to be slightly more extreme. The switching pattern of the resultant aerodynamic force is also readily apparent (see Fig. 8).

Discussion

Comparing the simulation lift and thrust forces for the forced-wing condition with those for the free-wing condition, which in turn are compared with the experimental data relevant to each condition, the lift on the downstroke appears to correlate well, whereas the lift on the upstroke is in excess of the experimental results. The effects of flexibility alone do not, therefore, account for the discrepancy between experimental data and data derived from a forced-wing representation. Admittedly the horizontal forces do not correlate as well as the vertical forces; the former, however, are of a lower order of magnitude and as such are not as significant.

To obtain a better correlation, the effects of leading-edge suction/separation in conjunction with flexibility need to be investigated. Leading-edge effects may lower the force on the downstroke and increase the force on the upstroke because of the torsional effects of flexibility. The present discrepancies may well be attributed to the absence of leading-edge suction/separation.

On the supination/downstroke segment of the wing beat, the chance of separation is reduced (with α_{le} relatively small), and as such leading-edge forces are likely to reduce the lift while simultaneously increasing the thrust because of the overall attitude of the wing. In the pronation/upstroke segment of the wing beat (with α_{le} relatively large), the chance of separation is increased, and as such the Polhamus analogy may be invoked whereby the leading-edge force is effectively rotated by 90 deg. [A theory used to account for the effect of any leading-edge bubble has been proposed by Polhamus.[27] According to the Polhamus analogy, the suction force is equated with the theoretical leading-edge singularity for thin wings in potential flow but is assumed to act primarily over the upper surface of the wing (i.e., rotated by 90 deg at the leading edge), thus giving rise to the characterization vortex lift.] In conjunction with the overall attitude of the leading edge of the wing (as in the case of the supination segment), the Polhamus analogy is likely to contribute both to an increase in lift and an increase in thrust, depending on the section of the wing before or after the station along the leading edge where separation occurs. Such hypotheses indicate that future studies should investigate the effects of leading-edge suction/separation.

It is evident that in both the forced- and free-wing conditions, the direction of the resultant aerodynamic force over each wing-beat cycle manifests a switching pattern coincident with the pronation and supination segments of the wing-beat cycle (the slight discrepancy between the simulation and experimental results may be attributed to the neglect of leading-edge suction/separation as well the assumptions made in modeling the combined wing structure). This switching phenomenon, comparable to that of bang-bang controllers found in optimal control systems, effectively decouples the magnitude from the direction of the resultant aerodynamic force within each wing-beat cycle and points to a means whereby control of the resultant aerodynamic force (its magnitude and direction) is achieved with flapping wings.

In this particular study the switching directions within each wing-beat cycle appear to be diametrically opposite one another, thus effectively resulting in a net aerodynamic force acting in the direction dictated by the supination segment of the wing beat (the mean magnitude of the aerodynamic force over the supination segment

of the wing beat being larger than that over the pronation segment of the wing beat). With the moth tethered, it can only be surmised that the dictated direction was also the moth's intended direction of travel were it untethered.

In addition, the free-wing condition results indicate that the structural aspects of the simulation free wing are too stiff. The excess stiffness could be a result of the blanket factor of 300 on the stiffness of the wing (as applied to the whole wing to account for wing corrugation), or to the assumption that the wings may be combined, or to the assumption that the root chord is completely rigid.

Conclusions

Improved correlation might be achieved if the following are done: 1) The effect of leading-edge suction/separation is included. 2) Rather than modeling the fore and aft wings as one combined wing, each is modeled separately. This would also have the added benefit of allowing the root angular motion of both fore and aft wings to be separated out. 3) More detailed finite element models of the fore and aft wings are constructed that would allow for the variation of stiffness as a result of wing corrugation. 4) Accurate root chord angular data for the fore and aft wings are gathered.

By excluding the wake from the analysis, only the bound circulation of the wing is brought into the calculation. The resultant aerodynamic loads are then far less than when the wake is included and do not correlate at all with experimental results (see Fig. 6). These results confirm the importance of including a comprehensive wake model in the unsteady aerodynamic analysis of beating wings.

Overall, the dynamic, kinematic, structural, and aerodynamic preliminaries and their synthesis are considered appropriate. Moreover, given the good correlations, the task of modeling the unsteady aerodynamics of a tethered moth's flapping wings is accomplished successfully using a panel method. This study has thereby established the importance of including the wake in analyses of the unsteady aerodynamics of flexible wings undergoing arbitrary, large-scale motion and has discovered a switching technique relevant to the control of the resultant aerodynamic force. It also points to the importance of including leading-edge effects and appropriate distributions of both mass and stiffness (including root connectivity) and confirms the utility of modeling naturally occuring modes of flapping flight.

The resultant simulation code has accounted for both the aerodynamic and inertial forces on flapping flexible wings in the presence of large-scale vortices. As such, the code is capable of contributing to an enriched understanding of the relationship between the trajectories, boundary shape, mass and stiffness distributions, and surface contouring of the wings and the gross movements of the host body. The code, therefore, lays important groundwork necessary for the establishment of the principles of FWT leading to the development of a versatile flight technology capable of much greater agility than either fixed- or rotary-wing technologies.

References

[1]Lippisch, A. M., "Man-Powered Flight in 1929," *Journal of the Royal Aeronautical Society*, Vol. 64, July 1960, pp. 395–398.

[2]Brooks, A. N., MacCready, P. B., Lissaman, P. B. S., and Morgan, W. R., "Development of a Wing-Flapping Flying Replica of the Largest Pterosaur," AIAA Paper 85-1446, July 1985.

[3]DeLaurier, J. D., and Harris, J. M., "A Study of Mechanical Flapping-Wing Flight," *Aeronautical Journal*, Vol. 97, Oct. 1993, pp. 277–286.

[4]DeLaurier, J. D., "An Ornithopter Wing Design," *Canadian Aeronautics and Space Journal*, Vol. 40, March 1994, pp. 10–18.

[5]Smith, M. J. C., "Simulating Flapping Insect Wings Using an Aerodynamic Panel Method: Towards the Development of Flapping-Wing Technology," Ph.D. Dissertation, School of Aeronautics and Astronautics, Purdue Univ., West Lafayette, IN, 1995.

[6]Smith, M. J. C., Wilkin, P. J., and Williams, M. H., "The Advantages of an Unsteady Panel Method in Modelling the Aerodynamic Forces on Rigid Flapping Wings," *Journal of Experimental Biology*, Vol. 199, May 1996, pp. 1073–1083.

[7]Vest, M. S., and Katz, J., "Unsteady Aerodynamic Model of Flapping Wings," AIAA Paper 95-0747, Jan. 1995.

[8]Spedding, G. R., "The Aerodynamics of Flight," *Advances in Comparative and Environmental Physiology*, edited by R. McNeal Alexander, Vol. 11, Springer–Verlag, Berlin, 1992, pp. 51–111.

[9]Phlips, P. J., East, R. A., and Pratt, N. H., "An Unsteady Lifting Line Theory of Flapping Wings with Application to the Forward Flight of Birds," *Journal of Fluid Mechanics*, Vol. 112, Nov. 1981, pp. 97–125.

[10]Betteridge, D. S., and Archer, R. D., "A Study of the Mechanics of Flapping Flight," *Aeronautical Quarterly*, Vol. 25, May 1974, pp. 129–142.

[11]Lan, C. E., "The Unsteady Quasi-Vortex-Lattice Method with Applications to Animal Propulsion," *Journal of Fluid Mechanics*, Vol. 93, Pt. 4, 1979, pp. 747–765.

[12]Azuma, A., "Local Momentum and Local Circulation Methods for Fixed, Rotary and Beating Wings," Inst. of Interdisciplinary Research, Faculty of Engineering, Univ. of Tokyo, Japan, Aug. 1983.

[13]Wilkin, P. J., and Williams, M. H., "Comparison of the Aerodynamic Forces on a Flying Sphingid Moth with Those Predicted by Quasi-Steady Theory," *Journal of Physiological Zoology*, Vol. 66, No. 6, 1993, pp.1015–1044.

[14]Lighthill, M. J., "The Inaugural Goldstein Memorial Lecture—Some Challenging New Applications for Basic Mathematical Models in the Mechanics of Fluids That Were Originally Pursued with Aeronautical Aims," *Aeronautical Journal*, Vol. 94, Feb. 1990, pp. 41–52.

[15]Ellington, C. P., "The Aerodynamics of Hovering Insect Flight," *Philosophical Transactions of the Royal Society of London*, Series B, Vol. 305, No. 1122, 1984, pp. 1–181.

[16]Jensen, M., and Weis-Fogh, T., "Biology and Physics of Locust Flight. V. Strength and Elasticity of Locust Cuticle," *Philosophical Transactions of the Royal Society of London*, Series B, Vol. 245, No. 721, 1962, pp. 137–169.

[17]Anon., "An Illustrated Glossary of Terms Used in 'Flight'," *Flight*, Vol. 1, No. 8, 1909, pp. 103, 104.

[18]Kawachi, K., "An Extension of the Local Momentum Theory to a Distorted Wake Model of a Hovering Rotor," NASA TM 81258, Feb. 1981.

[19]Friedmann, P. P., "Formulation and Solution of Rotary-Wing Aeroelastic Stability and Responce Problems," *Vertica*, Vol. 7, No. 2, 1983, pp. 101–141.

[20]Katz, J., and Plotkin, A., "Low-Speed Aerodynamics: From Wing Theory to Panel Methods," McGraw–Hill, San Francisco, CA, 1991.

[21]Ashby, D. L., Dudley, M. R., and Iguchi, S. K., "Development and Validation of an Advanced Low-Order Panel Method," NASA TM 101024, Oct. 1988.

[22]Bathe, K. J., Wilson, E. L., and Peterson, F. E., "SAP IV: A Structural Analysis Program for Static and Dynamic Response of Linear Systems," Univ. of California, EERC 73-11, Berkeley, CA, June 1973.

[23]Rees, C. J. C., "Form and Function in Corrugated Insect Wings," *Nature*, Vol. 256, July 1975, pp. 200–203.

[24]Harder, R. L., and Desmarais, R. N., "Interpolation Using Surface Splines," *Journal of Aircraft*, Vol. 9, Feb. 1972, pp. 189–191.

[25]Appa, K., "Finite Surface Spline," *Journal of Aircraft*, Vol. 26, May 1989, pp. 495, 496.

[26]Rees, C. J. C., "Aerodynamic Properties of an Insect Wing Section and a Smooth Aerofoil Compared," *Nature*, Vol. 258, Nov. 1975, pp. 141, 142.

[27]Polhamus, E. C., "Predictions of Vortex-Lift Characteristics Based on a Leading-Edge Suction Analogy," *Journal of Aircraft*, Vol. 8, April 1971, pp. 193–199.